

● *Original Contribution*

ON THE DIFFERENCES BETWEEN TWO-DIMENSIONAL AND THREE-DIMENSIONAL SIMULATIONS FOR ASSESSING ELASTOGRAPHIC IMAGE QUALITY: A SIMULATION STUDY

ABHAY V. PATIL,^{*,‡} THOMAS A. KROUSKOP,[†] JONATHAN OPHIR,^{*} and
SESHADRI SRINIVASAN^{*}

^{*}University of Texas Medical School, Department of Diagnostic and Interventional Imaging, Ultrasonics Laboratory, Houston, TX, USA; [†]Baylor College of Medicine, Houston, TX, USA; and [‡]University of Virginia, Biomedical Engineering, Charlottesville, VA, USA

(Received 18 March 2007; revised 10 November 2007; in final form 12 December 2007)

Abstract—In this work, we introduced an elastographic simulation framework, which estimates upper bounds on elastographic image quality by accounting for three-dimensional (3D) tissue motion and the 3D nature of the ultrasound beam. For the boundary conditions and the range of applied strains considered in this study, it was observed that for applied strains smaller than 0.7%, fast two-dimensional (2D) simulations and 3D simulations predicted similar upper bounds on elastographic signal-to-noise (SNR_e) and contrast-to-noise ratios (CNR_e); however, for applied strains greater than 0.7%, the predictions by 2D simulations grossly overestimated the achievable results when compared with upper bound results from 3D simulations. It was also found that linear increments in the elevational-to-lateral beamwidth ratio (beam ratio) resulted in nonlinear degradation in the achievable upper bounds on elastographic signal-to-noise ratio. For the modulus contrast ratio of ten between the target and the background, the peak difference in the prediction of contrast-to-noise by 2D and 3D simulations was approximately 10 dB, whereas, for modulus contrast ratio of 1.5, the peak difference increased to approximately 30 dB. No significant difference was observed between the spatial resolution predicted by 2D and 3D simulations; however, increase in beam ratio resulted in decrease in target detectability, especially at lower modulus contrast ratios. (E-mail: avpatil@virginia.edu) Published by Elsevier Inc. on behalf of the World Federation for Ultrasound in Medicine & Biology.

Key Words: 3D tissue motion, Elastography, Cross-correlation, Ultrasound, Image quality, Strain filter, 3D lesion models, 3D simulation framework, Elastographic simulations.

INTRODUCTION

Pathologic changes in soft tissues are often correlated with changes in the tissue mechanical properties, such as the elastic modulus (Fung 1981; Krouskop 1998). In many cases, these pathologic changes do not significantly alter the echogenicity of the tissue and may, therefore, go undetected in normal B-mode ultrasound scans. However, they may be detected by imaging the mechanical properties of a tissue or its associated strain field, as in elastography (Ophir et al. 1991; O'Donnell et al. 1994). In elastography, external compressions are applied to a tissue to estimate its stiffness; the resulting

tissue motion (or displacement) is then estimated by tracking the pre- and postcompression echo radio-frequency (RF) data. The gradient of the estimated internal displacement image yields an elastogram or a strain image.

Image formation in ultrasound is a complex interplay of parameters including the pulse width, the pulse shape, ultrasonic array geometry and associated optimization parameters such as the type of aperture/apodization, the type of transmit and receive focusing, phase-correction, system frame rate *etc.* Optimization of any of these parameters is desirable and is contingent upon the type of application (cardiac imaging, abdominal imaging *etc.*). A variety of simulation models (Jensen et al. 2000; Ranganathan et al. 2007) have been proposed by various researchers to address these issues, which may be indispensable in designing an optimized application-specific scanning system.

Address correspondence to: Abhay V. Patil, University of Virginia, Biomedical Engineering, 415 Lane Road, MR5, Room 2117, Charlottesville, VA 22903, USA. E-mail: avpatil@virginia.edu

In elastography, the image formation process is not only a function of the ultrasonic parameters but also of the mechanical (*e.g.*, boundary conditions) and signal processing (*e.g.*, processing window size) parameters. Changes in the boundary conditions can change the information obtained from an elastogram. For example, mechanical artifacts such as target-hardening and stress concentrations have been reported in the literature (Ponnekanti et al. 1995), which are functions of the compressor type and are independent of the ultrasound system and the signal processing parameters used to collect and analyze the data. Also, the tissue motion under the influence of an external stress is inherently 3D and the influence of the elevational or out-of-plane tissue motion on elastographic image quality is significant. The slice thickness or the elevational extent of the ultrasonic beam is fixed and in turn limits the elevational resolution/signal-to-noise ratio of a system. Narrower elevational beam widths result in a finer elevational resolution but may cause a higher signal decorrelation of tracked pre- and postcompression signals and correspondingly lower signal-to-noise and contrast-to-noise ratios and *vice versa*. Previously proposed elastographic simulation frameworks (Righetti and Ophir 2002; Righetti et al. 2003; Srinivasan et al. 2003) assumed plane strain conditions and flat ultrasonic beam widths, thus constraining the three-dimensional (3D) problem to two-dimensional (2D). Kallel and Ophir (1996) used a 3D analytical model for estimating tissue scatterer motion in response to an external displacement field; their model assumed lower applied strains ($\leq 1\%$) and did not account for shear or rotation of the tissue scatterers, thus limiting its application. As previously stated, elastography is inherently a 3D problem because the motions being tracked occur in three dimensions, the targets are 3D and the ultrasound beam profiles are 3D (Konofagou and Ophir 2000). Thus, from the above discussion it is obvious that the elastographic image quality estimated using models that account for various 3D factors will predict inferior image quality than those models which account for 2D factors only. However, in this work we seek to determine a set of threshold parameters or factors, below which fast 2D simulations may predict acceptable results, *i.e.*, statistically insignificant difference between 2D and 3D model predictions. To test the above hypothesis, we quantified the differences in the upper bounds of elastographic image quality that result from modeling the tissue motion and the ultrasound beam as 3D versus 2D. The differences in the image quality are quantified in terms of signal-to-noise ratio and strain filter theory (Céspedes and Ophir 1993; Varghese and Ophir 1997b). We also examined the differences in image contrast introduced by modeling lesions (targets) as 3D entities instead of 2D entities. Upper bounds on lesion detect-

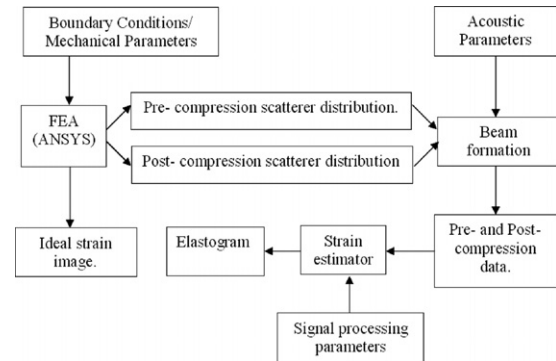


Fig. 1. A block diagram representation of the framework for performing three-dimensional elastography simulations.

ability (3D versus 2D) for varying modulus contrasts are examined and quantified in terms of contrast-to-noise ratios (Bilgen and Insana 1997) and spatial resolution (Righetti et al. 2002; Srinivasan et al. 2003).

METHODS

The simulation framework

Figure 1 illustrates a block diagram of the methodology for the simulation framework used in this work. The framework can be briefly divided into three blocks: the mechanical, the ultrasonic and the signal processing blocks. In this work, we have used finite element based numerical simulations to estimate the scatterer motion. ANSYS (Canonsburg, PA, USA), a finite element analysis (FEA) software, was used to simulate the internal displacement field produced by an externally applied strain. Using the FEA software, 3D scatterer motion under a variety of boundary conditions (uniform or non-uniform) can be simulated with a high degree of precision. In this work, all 3D FEA simulations were performed using slip boundary conditions, where the model is allowed to slip in azimuth and elevation *i.e.*, the motion of the tissue scatterers is unconstrained in these directions. External compressions were applied to the top surface of the FEA model in the axial direction. In the case of 2D simulations, the model was unconstrained in the lateral (azimuth) direction and external compressions were applied to the top edge of the 2D FEA model. The constitutive equations used by an FEA solver for solving a small displacement linear elastic problem have been discussed in detail in Sadda (1974). For this work, preconditioned conjugate gradient iterative solver was used to solve the elasticity equations to obtain the numerical estimate of the internal displacement field (Elman et al. 1989). All FEA simulations were performed at a FEA node density of 13 nodes per ultrasonic resolution cell (Patil et al. 2007).

It is well known that elastograms have space vary-

Table 1. Specifications for SNRe study

Young's modulus	100 KPa
Window size (W)	2 mm
Window shift (ΔW)	5%
Center frequency	5 MHz
Sampling frequency	48 MHz
Bandwidth	50% fractional
Lateral pitch	0.4 mm
Elevational pitch	0.9 mm
Lateral beam-width	1 mm
Elevational beam-width	1 mm
1D array	100 A-lines
1.5D array	100 A-lines per plane, 9 planes
Size of 2D-phantom	40 × 40 mm
Size of 3D-phantom	40 × 40 × 40 mm

ing or nonstationary (Varghese and Ophir 1997a) image quality that is determined by a number of different ultrasonic parameters. However, for this work, we focused on the differences between the upper bounds of 2D and 3D models and hence, we restricted our analyses to the focus or focal-plane, where the assumption of a shift-invariant impulse response is applicable (Bamber and Phelp 1977). However, predictions for the degradation in elastographic image quality due to spatially varying ultrasonic parameters are discussed in later sections of this manuscript. For a tissue modeled as an ensemble of scatterers in a 3D space with random scattering amplitude, the precompression echo RF (radio-frequency) data can be represented as a convolution of the tissue scatterer function and the interrogating PSF (point spread function). The postcompression tissue scatterer function is obtained by redistributing the tissue scatterers based on the 2D/3D displacement field obtained from the FEA simulation. For lower strains, less than 1%, the tissue scatterer motion is predominantly translational (Kallel and Ophir 1996). However, at higher strains and for nonslip boundary conditions at the edges of the model, the shear component is substantial (Thitaikumar *et al.* 2005) and these effects can be modeled in the FEA simulations used in this work. Analytically, the pre- and postcompression echo RF data are represented as (*e.g.*, Konofagou and Ophir 2000):

$$r_1(x, y, z) = p(x, y, z) \otimes t_{pre}(x, y, z) + n_1(x, y, z), \quad (1)$$

$$r_2(x, y, z) = p(x, y, z) \otimes t_{post}(x, y, z) + n_2(x, y, z). \quad (2)$$

Where x , y , z and z are lateral, axial, and elevational directions, $r_1(x, y, z)$ is the precompression RF signal, $r_2(x, y, z)$ is the postcompression RF signal, $p(x, y, z)$ is the PSF or the system point spread function, $t_{pre}(x, y, z)$ is the precompression tissue scatterer function, $t_{post}(x, y, z)$ is the tissue scatterer function obtained by redistributing the scatterers to the displacement fields obtained

from the 3D numerical simulations, $n_1(x, y, z)$ and $n_2(x, y, z)$ are two renditions of uncorrelated random noises.

The PSF was modeled as a sinusoidal pulse with a Gaussian envelope (Konofagou and Ophir 2000)

$$p(x, y, z) = \exp\left(-\left(\frac{x^2}{\sigma_x^2} + \frac{y^2}{\sigma_y^2} + \frac{z^2}{\sigma_z^2}\right)\right) \sin\left(\frac{2\pi * y}{\lambda}\right), \quad (3)$$

where σ_x is the lateral correlation length,

σ_y is the axial correlation length,

σ_z is the elevational correlation length,

and λ is the center wavelength.

It is important to note that parameters in eqns 1, 2 and 3 can be adjusted to generate a focused beam with a desired beamwidth and depth of field. Also, since this is a 3D convolution model, it results in a uniform image quality throughout the generated elastogram. As previously stated, a 3D convolution model was used as the analyses were restricted to the focus or focal plane.

A variety of strain reconstruction algorithms have been proposed for reconstructing the internal tissue strain from a set of pre- and postcompression echo RF data (Viola and Walker 2005; Chatrurvedi and Insana 1998). For this work, we used the strain estimation algorithm proposed by Srinivasan *et al.* (2002a, 2002b). In the algorithm of Srinivasan *et al.*, tracking is performed in two stages: (1) the global stretching stage and (2) the local tracking stage. In the global tracking stage, the postcompression data are globally stretched by the applied strain and tracked to estimate strain over a tracking window. In the second stage, the stretching operation is performed at the local window level. A postcompression window data are stretched by the minimum of the applied global strain and the first stage local window estimate, and tracked. The displacements from the both stages are added and differentiated to yield a strain elastogram. The simulation parameters used in this work are listed in Tables 1, 2 and 3.

Elastographic simulations for upper bound estimation

Comparison of the signal-to-noise ratios (SNR_e) for the two cases. The 2D and 3D finite element (FEA) simulations were performed using the specifications listed in Table 1. For the 2D simulations, the ROI was a

Table 2. Mechanical models for CNRe study

Size of 2D-phantom	40 × 40 mm
Radius of the cylindrical inclusion (2D-phantom)	2.5 mm
Size of 3D-phantom	40 × 40 × 40 mm
Radius of the spherical inclusion (3D-phantom)	2.5 mm
Young's modulus in background (2D and 3D)	100 KPa
Young's modulus in inclusion (2D and 3D)	150 ~ 1000 KPa

Table 3. Specifications for spatial resolution study

Young's modulus in background (2D and 3D)	100 KPa
Young's modulus in the inclusion (2D and 3D)	300 KPa
Size of the phantom (2D)	20 × 20 mm
Size of phantom (3D)	20 × 8 × 20 mm
Size of the inclusions (2D and 3D)	1.5 mm
Window (W)	2.5 times wavelength
Window shift (ΔW)	10%
Center frequency	2.5, 5, 7.5 and 10 MHz
Sampling frequency	10 times the center frequency
F-Number	1
Bandwidth	80%
1D linear array transducer	100 A-lines
1.5D linear array transducer	100 A-lines, (34 scan planes)

40 × 40 mm plane having uniform stiffness (100 KPa), with slip boundary conditions on the bottom and unconstrained displacements on the sides. Uniform external compression was applied from the top. For 3D FEA simulations, the ROI was a 40 × 40 × 40 mm cube with uniform stiffness of 100 KPa. The cube was compressed uniformly from the top along the axial direction. The motions in the elevational and lateral directions of all points inside the ROI were unconstrained. All FEA simulations were conducted for a range of applied strains varying from 0.01% to 10%. The FEA calculated local displacement fields were applied to the tissue scatterers to simulate motion of the tissue scatterers due to an applied displacement. The pre- and the postcompression RF data were then generated using eqns 1, 2 and 3. For a comprehensive analysis of the effects of 3D tissue motion on the elastographic image quality, we investigated:

- (1) The achievable upper bounds of the elastographic image quality as the distance of scan plane increased away from the plane of elevational symmetry.
- (2) The variation in the upper bounds of the elastographic image quality caused by varying the elevational thickness of the beam width.

The simulated pre- and the postcompression RF data obtained for the 2D and 3D cases were tracked using the algorithm proposed by Srinivasan et al. (2002a, 2002b). The strain images generated from the 2D and 3D simulations were compared using the signal-to-noise ratio, contrast-to-noise ratio (CNR_e) and spatial resolution measures of image quality. The signal-to-noise ratio (Céspedes and Ophir 1993) was evaluated using the following expression

$$SNR_e = \frac{s}{\sigma_s}, \quad (4a)$$

$$\sigma_s = \frac{2\sigma_t^2}{T\Delta T} \quad (4b)$$

where s is the average estimated strain and σ_s is the standard deviation of the strain estimates, T is the tracking window and ΔT is the shift. An unbiased estimation of elastographic SNR_e (Srinivasan et al. 2002c) was obtained by calculating the strain variances from the correlation coefficients obtained by tracking the pre- and postcompression RF data. The expression for calculating the displacement variances directly from the cross-correlation coefficient is derived in (Walker and Trahey 1995 and Céspedes et al. 1997) and is stated as follows

$$\sigma_t^2 \cong \frac{3}{\pi^2 T (B^3 + 12Bf_o^2)} \left[\frac{1}{\rho^2} \left(1 + \frac{1}{SNR_s} \right)^2 - 1 \right], \quad (5)$$

where T , B and f_o are the observation window length ($W = Tc/2$), the absolute system bandwidth and the center frequency, respectively; c is the velocity of sound through the tissue. SNR_s is the system signal-to-noise ratio and ρ is the cross-correlation coefficient, which is estimated directly from the tracking algorithm. The values of different parameters (in eqn 5) used in our simulations are listed in Table 1. Frequency-dependent attenuation is not addressed in these analyses. However, the expected increase in the lower bound on the variances in strain estimation (hence, degradation in the upper bound of the signal-to-noise ratio), for both the 2D and 3D cases, due to frequency-dependent attenuation can be estimated using the expression derived in (Varghese and Ophir 1997a) and is stated as follows:

$$SNR_{ATTENUATION}(y) = SNR_s \sqrt{\frac{1}{\sqrt{\eta}} \exp\left(-\left[\frac{(f_o - \xi n f_o^{n-1})^2}{2n\sigma_f^2} - \frac{f_o^2 \xi(n-1)f_o^n}{2\sigma_f^2}\right]\right)}, \quad (6)$$

Where

$$\eta = 1 + 2\sigma_f^2 \alpha_o y (n-1) f_o^{n-2} \quad (7a)$$

and

$$\xi = 2\sigma_f^2 \alpha_o (2-n)y. \quad (7b)$$

Where, y is the axial depth from the surface of the transducer, α_o is the attenuation coefficient of the medium, σ_f^2 is the variance of the PSF spectrum, f_o is the center frequency of the scan, and n is the exponent of frequency dependence form $a(f) = a_0 f^n$. Thus, the estimated upper bounds obtained from our simulations can be analytically scaled using eqns 5 through 7b to account for the effect of the frequency-dependent attenuation; the scaled upper bound will then represent the combined

effect of the 3D tissue motion and frequency-dependent attenuation at any desired depth.

Comparison of the CNR_e for the two cases. The 2D and 3D finite element simulations were conducted using the specifications listed in Table 1 and Table 2. For the 2D simulations, the ROI was a 40×40 mm plane with a circular inclusion (cross section of a cylinder) of diameter 5 mm. The stiffness of the background was 100 KPa and was constant for all cases. Lesion detectability for 3D versus 2D cases was evaluated by estimating the contrast transfer efficiency-CTE (in terms of CNR_e for given modulus contrasts) for two different geometries (sphere-3D versus cylinder-2D). Inclusions with four different modulus contrast were considered in the simulations; the stiffness of the inclusion was varied from 150, 300, 700 to 1000 KPa. For the 3D simulations, the ROI was a $40 \times 40 \times 40$ mm³ volume; the enclosed inclusion was a sphere with a 5 mm diameter centered in the volume. Boundary conditions for this study were same as those discussed in the signal-to-noise ratio study. Simulations were conducted for a range of induced strain from 0.01% to 10%. The contrast-to-noise ratio (CNR_e) was calculated from the elastograms as a Fisher's discriminant function (Bilgen and Insana 1997).

$$CNR_e = \frac{2(s_i - s_b)^2}{(\sigma_i^2 + \sigma_b^2)}. \quad (8)$$

In eqn 8, σ_i is the standard deviation of the strain estimates in the inclusion, σ_b is the standard deviation of the strain estimates in the background, s_i is the average estimated strain in the inclusion and s_b is the average estimated strain in the background. Variances were estimated from the cross-correlation coefficient (Srinivasan *et al.* 2002c) using eqns 4a, 4b and 5. A plot of the variations in elastographic contrast-to-noise ratio as a function of the applied strain is referred to as the CNR_e plot or CNR_e curve in this manuscript. The upper bound on CNR_e for the four modulus contrast ratio cases studied in this work were computed and compared for the 2D versus 3D cases.

Comparison of the spatial resolutions for the two cases. The spatial resolution study had three components:

- (1) Comparison of the axial and the lateral resolution of the 2D and 3D case.
- (2) Estimation of the elastographic elevational resolution of the axial elastograms obtained for the 3D case.
- (3) The effect of varying the elevational beam-thickness on the estimated spatial resolution.

The specifications for the resolution study are listed

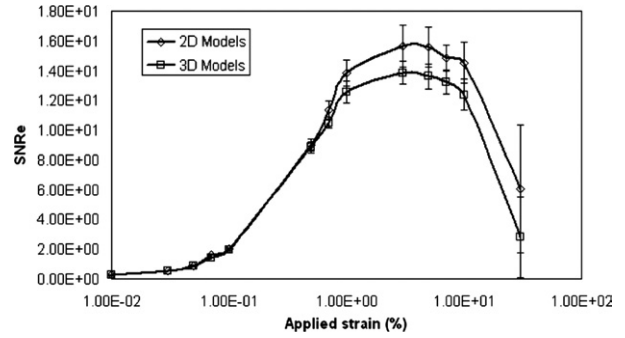


Fig. 2. Simulated strain filters obtained for the two-dimensional and three-dimensional (central scan plane) cases.

in Table 3. The resolution study was carried out at four center frequencies (2.5, 5, 7.5 and 10 MHz) with a relatively low modulus contrast of three. Axial, lateral and elevational elastographic resolutions were estimated from the simulations using the method and criterion proposed by Righetti *et al.* (2002, 2003). The beam-ratio (elevational beam thickness to lateral beam thickness) for the spatial resolution study was increased from 1 to 2, and was performed to quantify the degradation in the axial, lateral and elevational resolution of an elastogram due to an increase in the slice thickness. The analytical expressions for elastographic axial and lateral resolutions have been derived by Srinivasan *et al.* (2003) and can be stated as follows

$$R_0 = k(W + \Delta W), \quad W > \frac{hc}{3B}, \quad (9)$$

$$R_1 = kB_1, \quad R_1 > \frac{B_1}{1.5}, \quad (10)$$

where W is the window length in mm, h is a constant its value is 5, B is the absolute bandwidth and c is the velocity of sound through the tissue, B_1 is the lateral beamwidth in mm and k is a constant and was 0.5 for our studies.

RESULTS AND DISCUSSION

Figure 2 illustrates the strain filter plots obtained for the 2D and the 3D cases. As discussed in the previous sections, the strain filter is defined as the plot of elastographic signal-to-noise ratio as a function of applied strain (Varghese and Ophir 1997b). The strain filter of the 3D case was calculated at the central elevational scan plane (assuming elevational symmetry). Note that the strain filter for the 3D case is consistently lower than the corresponding strain filter for the 2D case; the differences in the estimated signal-to-noise ratio between the 2D and 3D cases is increased for higher strains (typically

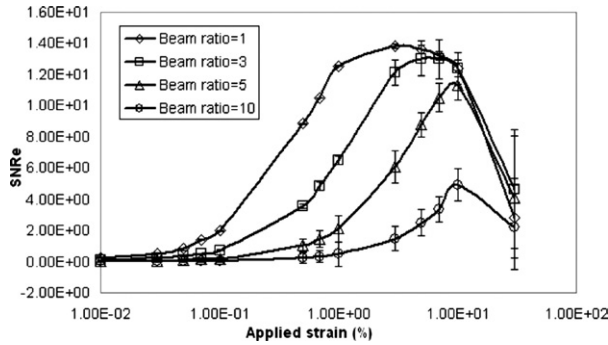


Fig. 3. Effect of the beamwidth ratio on the simulated strain filters obtained for the three-dimensional case from the central elevational plane.

>1%) and is probably due to increased scatterer motion in and out of the scan plane. At lower strains (<1%), the scatterer motion is predominantly translational (Kallel and Ophir 1996). The shear component in the scatterer motion increases with increase in tissue strain, and with added dimensionality (3D versus 2D) the affect of the shear motion substantially amplifies and is partially responsible for a greater differences between the two strain filters (Thitaikumar et al. 2005). Fisher's ANOVA was used to test the significance of the differences between the strain filters obtained from the 2D and 3D cases. For applied strains above 0.7%, the strain filters (Fig. 2) for the 2D and the 3D cases were found to be statistically different at a 95% confidence level (p -value = 0.05).

Figure 3 illustrates the degradation in the elastographic image quality at the elevational axis of symmetry with successive increases in the elevational beamwidth. The beamwidth ratio (elevational to lateral beam width) was gradually increased from 1 to 10, while the lateral beam width was kept constant (to study the effect of slice thickness on the image quality) at 1 mm. A family of strain filters

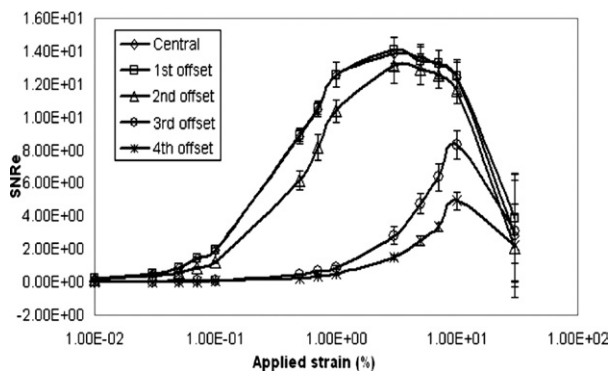


Fig. 4. Simulated strain filters obtained for the three-dimensional case from the central elevational and successive offset planes separated by elevational pitch of 0.9 mm.

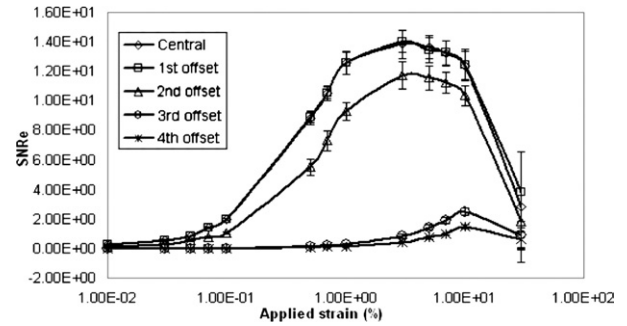


Fig. 5. Simulated strain filters obtained for the three-dimensional case from the central elevational and successive offset planes. The beamwidth ratio was 2; elevational pitch was 0.9 mm.

for the 3D cases was obtained from the central elevational plane. The elevational beamwidth is typically narrowest at the focus and spreads out as the distance from the focus increases. Therefore, the correlation length of the ultrasound beam in the elevational direction increases at points away from the focus. Wider correlation lengths in the elevational direction imply wider slice thickness and hence more nonuniform scatterer motion within the slice, which reduces the correlation coefficient of the pre- and the tracked postcompression data. Figure 3 gives insight into the deterioration of the elastographic image quality in the regions-of-interest that are not at the focus. The upper bounds are reduced causing a significant reduction in the dynamic range (-6 dB width or full width at the half maximum (FWHM) of the strain filter) of the strain filter by causing a shift in the peak of the strain filter to the right; this shift increases with increases in the elevational beamwidths. The strain filters can be further derated by accounting for the frequency-dependent attenuation (eqn 6). Based on the analysis of Varghese and Ophir (1997a) on frequency-

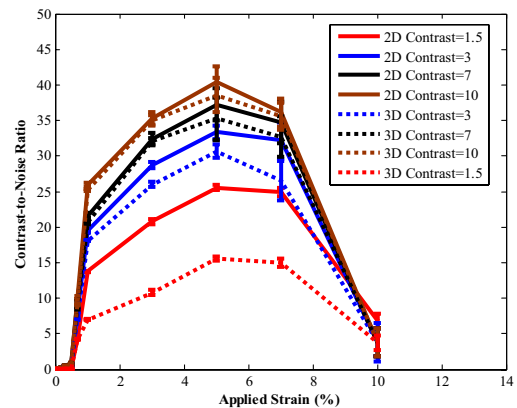


Fig. 6. Contrast-to-noise ratio plots obtained from two-dimensional (solid) and three-dimensional (dashed) cases for contrast ratio of 10, 7, 3 and 1.5.

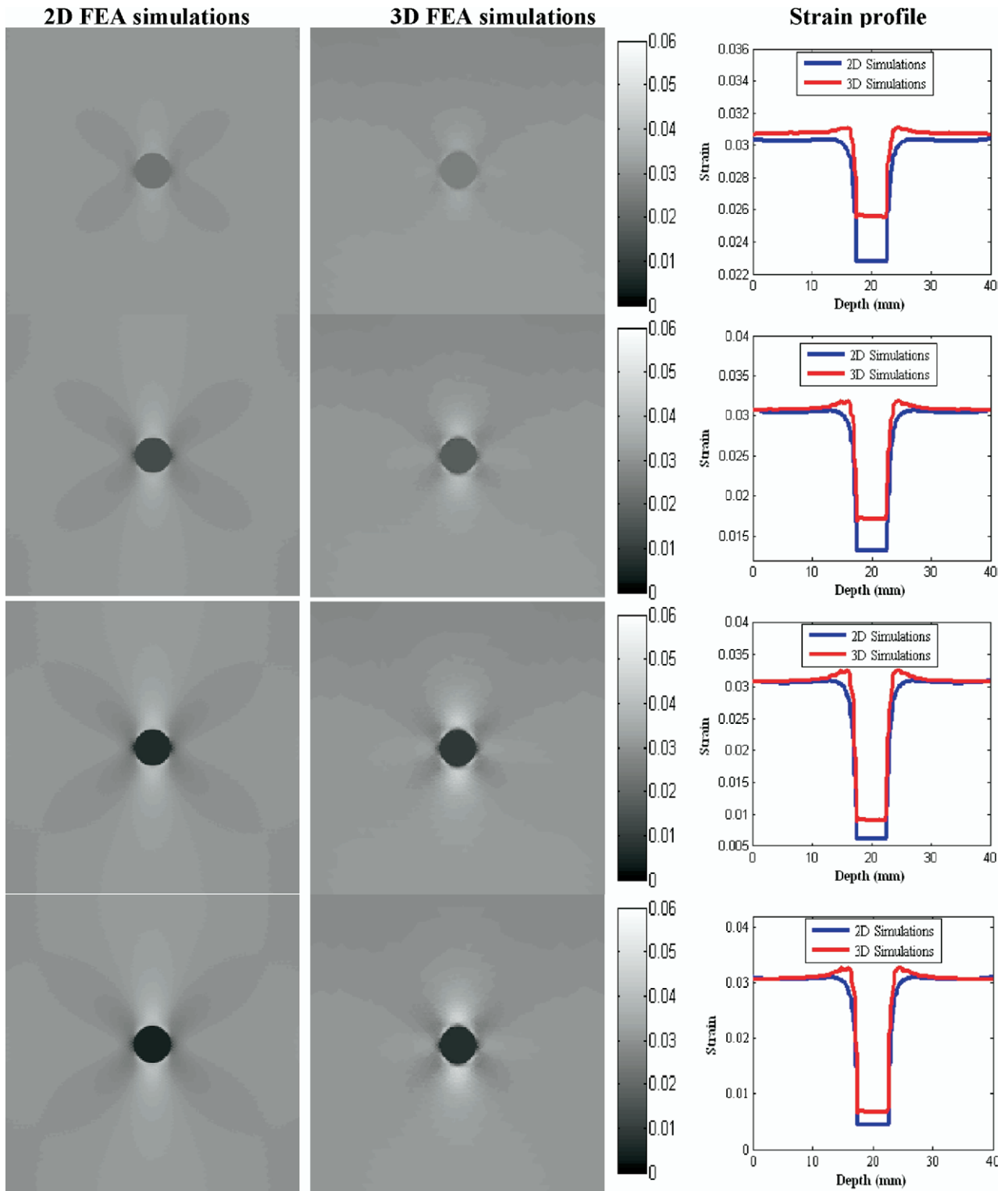


Fig. 7. Finite element analysis (FEA) solutions using three-dimensional and two-dimensional models and strain profiles over the depth of FEA models. Top row: Contrast of 1.5. Second row: Contrast of 3. Third row: Contrast of 7. Last row: Contrast of 10.

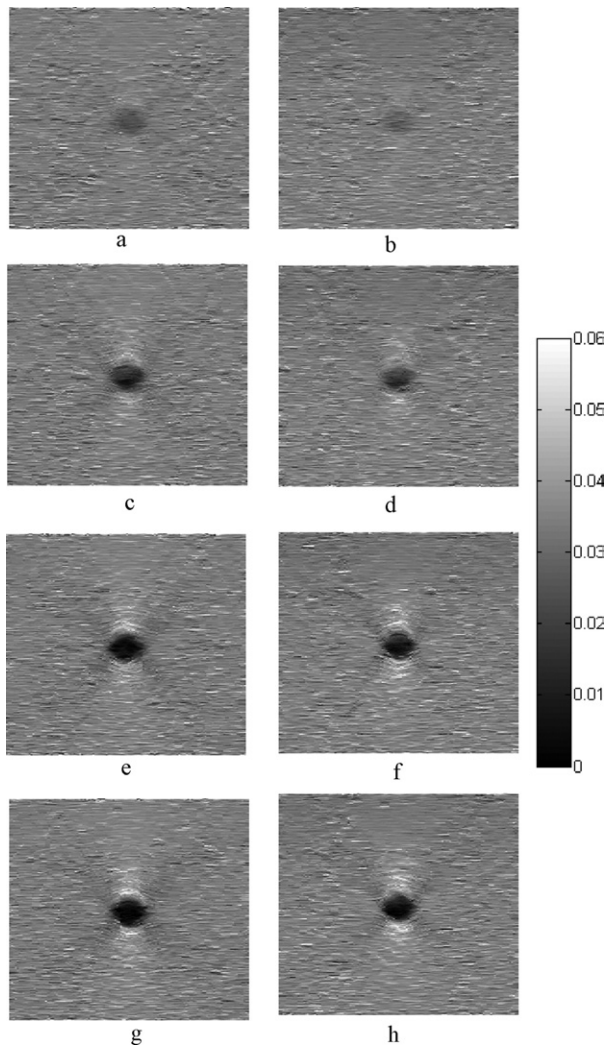


Fig. 8. (a) through (h): Elastograms from two-dimensional (a), (c), (e) and (g) and three-dimensional (b), (d), (f) and (h) cases. (a) and (b): Contrast of 1.5. (c) and (d): Contrast of 3. (e) and (f): Contrast of 7. (g) and (h): Contrast of 10.

dependent attenuation and its effects on the strain filter, we believe that the reduction in the dynamic range and sensitivity of the strain filter, with depth, will be nonlinear. An in-depth analysis of the frequency-dependent attenuation and its effect on elastographic image quality (in terms of strain filter theory) is provided by Varghese and Ophir (1997a).

Figure 4 illustrates a family of strain filters (3D case) obtained from the central elevational plane and from the successive offset planes separated by approximately three wavelengths (elevational pitch 0.9 mm). The upper bound deteriorates nonlinearly with increasing elevational distance of the scan plane from the central plane and we believe the deterioration is due to increased elevational motion of scatterers located away from the central scan plane; the degradation is further exaggerated by increases in the elevational

beamwidth as is illustrated in Fig. 5. It is well known that the relationship between the elastographic signal-to-noise ratio and cross-correlation coefficient is highly nonlinear (Varghese and Ophir 1996; Céspedes and Ophir 1993). Hence, a very small change in the cross-correlation coefficient causes large variations in the elastographic signal-to-noise ratio. For increasing beamwidths, the slope of the cross-correlation coefficient decay becomes steeper, which causes a faster reduction in the dynamic range (-6 dB width of the strain filter or the FWHM) of the strain filters, as in Fig. 5. The strain filters obtained from the central and the first offset plane (0.9 mm from the elevational axis of symmetry) were statistically similar to each other, whereas those obtained from the second and the successive offset planes were statistically different from each other (p -values = 0.05). It is worthwhile to note that the area under the strain filter obtained from different scan planes decreases nonlinearly as a function of the elevational distance of a scan plane from the elevational axis of symmetry. This demonstrates that there is a nonlinear reduction in elastographic image quality (defined as the area under the strain filter at a given resolution) with increasing separation between the scan plane and the axis of symmetry.

The CNR_e study was carried out at four different modulus contrast ratios, 1.5, 3, 7 and 10. Figure 6 illustrates the CNR_e curves obtained from the 2D and the 3D cases for the different modulus contrast values. Notice that there is a considerable difference in the CNR_e curves for the two cases and the difference increases as the modulus contrast decreases.

For the 3D case, the combination of elevationally wider beams and a spherical representation of the inclusion resulted in two visible effects: First, a reduced CNR_e was noted. This is caused by the lower contrast transfer efficiencies (Ponnekanti et al. 1995) of the 3D inclusion model (Fig. 7) and the elevational beamwidth of the ultrasound beam, which allows out-of-scan plane scatterer motion to corrupt the estimation of the in-plane scatterer motion. The effect is somewhat similar to the cystic fill-in effect that is sometime seen in sonograms (O'Donnell and Flax 1988). The second effect was the smaller measured inclusion size (data not shown) in the 3D cases due to the finite elevational beam dimensions that encompass the spherical inclusion (Fig. 8). Hence, the smallest lesion size detectable in the 2D case will be slightly smaller than that for the 3D case; enlarging the elevational beamwidth will further increase the detectable lesion size in an elastogram obtained from the 3D case. Hence, target detectability for the 3D case appears to be worse than for the 2D case, especially at broader elevational beamwidths and lower modulus contrast ratios.

Figure 9a illustrates the estimated axial resolution for the 2D and the 3D cases. The estimated axial resolution showed a dependence on the center frequency and was found to be approximately twice the central wave-

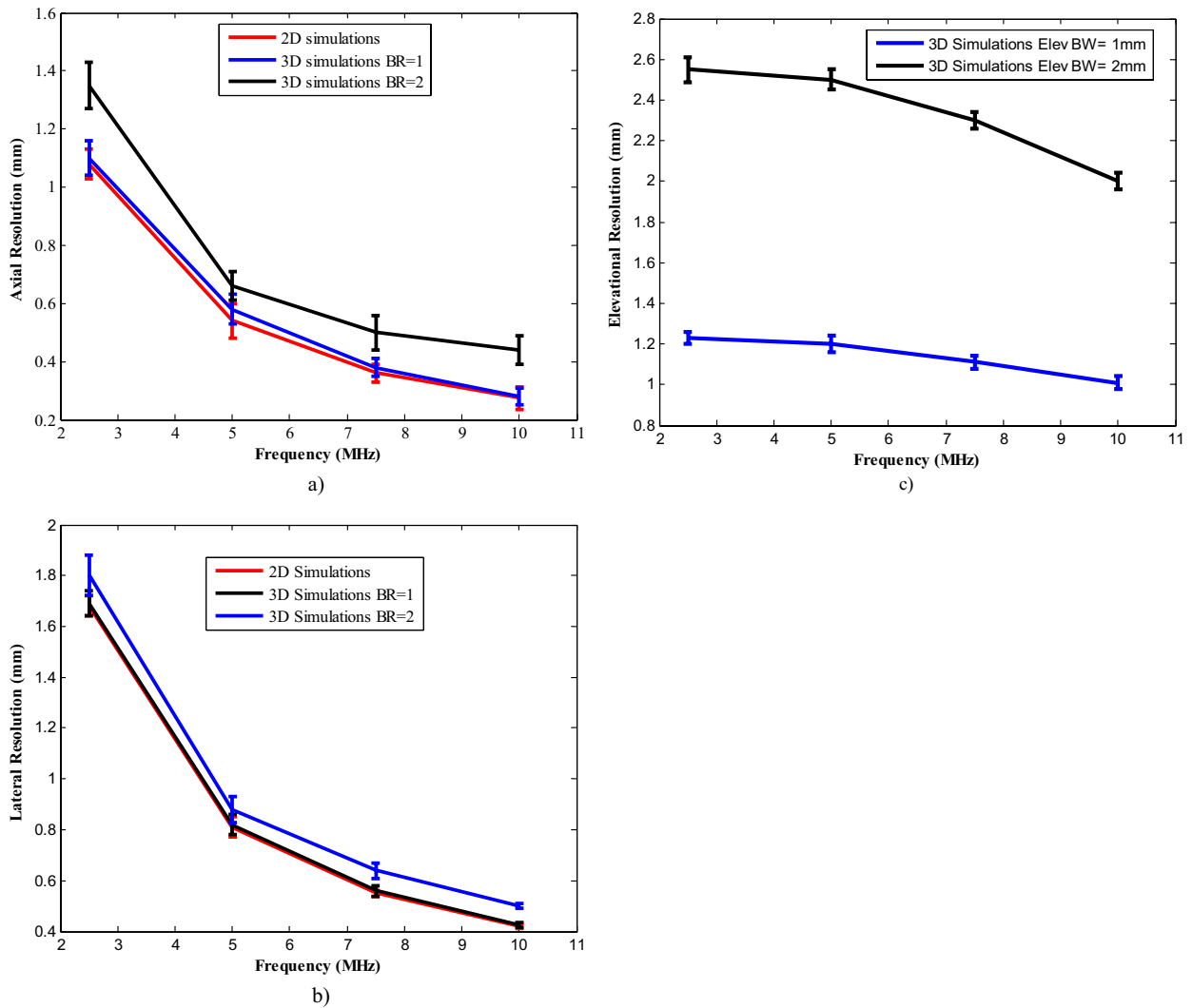


Fig. 9. (a) Axial resolution. (b) Lateral resolution. (c) Elevational resolution.

length for both the 2D and 3D model cases. However, there was no statistical difference (Fisher's ANOVA p -value = 0.05) between the estimated axial resolution of the 2D and the 3D cases (Fig. 9a). The lateral resolution showed a dependence on the greater of the lateral beamwidth and the lateral pitch (Fig. 9b), again no statistical difference was found between the estimated lateral resolution in the 2D and the 3D cases.

The axial and lateral resolutions for the 3D case deteriorated with increasing elevational beamwidth (Fig. 9a and b). The estimated axial- and lateral-resolutions for the 3D case, at a beamwidth ratio of 2, differed significantly (p -values = 0.05) from the estimated resolutions of the 2D cases (Fig. 9a and b). Thus, as previously noted, increasing elevational beamwidths decreases the probability of lesion detection (target detectability) and is apparent from the results of the contrast-to-noise ratio

and the spatial resolution studies. The estimated elevational resolution for 3D models is shown in Fig. 9c.

CONCLUSION

For high modulus contrast ratios (>7) and strains less than 0.7%, the upper bounds on the contrast-to-noise ratio and signal-to-noise ratio predicted by 2D and 3D simulations coincide. Hence, for these conditions, fast 2D simulations are sufficient. For higher applied strains ($>0.7\%$) and low modulus contrast ratios (<7), the 2D simulations grossly overestimated the achievable image quality. Hence, for these conditions, it may be advisable to use complete 3D elastographic simulations. No significant difference was observed between the spatial resolution estimated by 2D and 3D elastographic simulations. However, lesion or target detectability, (in terms of contrast-to-noise ratio and spatial

resolution) especially at lower modulus contrast, was found to be a function of elevational beamwidth. Thus, elevational beamwidth may set a lower bound on a smallest target discernable on an elastogram. Elastographic image quality deteriorated nonlinearly as a function of the scan plane away from the axis of elevational symmetry. The results predicted by this simulation framework can be derated analytically to account for the frequency-dependent attenuation. Given these facts, this framework may prove useful in performing simulations for a variety of techniques such as shear strain elastography and poroelastography. The 3D simulations framework may be powerful in the sense that it could be used to study the CTEs of different targets (and temporal strain behavior) with different boundary conditions, to study and identify the mechanical artifacts due to these different boundary conditions and suggest optimal image correction (strain normalization) techniques (Souchon et al. 2002), which may help in maximizing the achievable image contrast, without eliminating useful image information. To a first order, analytical derating factors may be used to estimate off focus image quality as suggested in this article. However, for studying a particular clinical problem (3D quantitative prostate cancer study *etc.* Patil et al. 2007) more evolved and sophisticated beam forming models should be used (Ranganathan et al. 2007). Nevertheless, the results of this work are expected to be applicable to the construction of real phantoms, where it is generally easier to manufacture phantoms that contain cylindrical inclusions. Such phantoms may turn out to not adequately represent the practical appearance of elastograms of 3D inclusions under certain conditions.

Acknowledgments—This work was supported in part by the program project grant PO1-CA64597 to the University of Texas Medical School at Houston, and by a paid Teaching assistantship to Abhay V. Patil by the University of Houston. Author Abhay V Patil is grateful to John A Hossack, and the Department of Biomedical Engineering at the University of Virginia for providing support (Army grant, W81XWH04-1-0240) during a long revision period of this paper.

REFERENCES

- Bamber JC, Phelp J. The effective directivity characteristic of a pulsed ultrasound transducer and its measurement by semi-automatic means. *Ultrasonics* 1977;15:169–174.
- Bilgen M, Insana MF. Predicting target detectability in acoustic elastography. *IEEE Ultrason Symp* 1997;2:1427–1430.
- Céspedes, E. I. and Ophir, J., Reduction of image noise in elastography. *Ultrasonic Imaging* 1993;15:89–102.
- Céspedes I, Ophir J, Alam SK. The combined effect of signal decorrelation and random noise on the variance of time delay estimation. *IEEE Ultrason Ferroelectr Freq Control* 1997;44:220–225.
- Chaturvedi P, Insana M, Hall T J. 2D-companding for noise reduction in strain imaging. *IEEE Ultrason Ferroelectr Freq Control* 1998;45:179–191.
- Elman HC, Argon E. Ordering techniques for preconditioned conjugate gradient method on parallel computers. *Comput Phys Commun* 1989;53:253–269.
- Fung YG. Biomechanical properties of the living tissue. New York: Springer, Chapter 7, 1981.
- Jensen JA, Nikolov S. Fast simulations of ultrasound images. *Proc IEEE Ultrason Symp* 2000;2:1721–1724.
- Kallel F, Ophir J. Three dimensional tissue motion and its effect on image noise in elastography. *Ultrasound Med Biol* 1996;22:463–470.
- Konofagou EE, Ophir J. Precision estimation and imaging of normal and shear components of the 3D strain tensor in elastography. *Phys Med Biol* 2000;45:1553–1563.
- Krouskop TA, Wheeler TM, Kallel F, Garra BS, Hall T. Elastic moduli of breast and prostate tissues under compression. *Ultrasonic Imaging*, 1998;20:260–274.
- O'Donnell M, Skovoroda R, Shapo BM, Emelianov Y. Internal displacement and strain imaging using ultrasonic speckles. *IEEE Ultrason Ferroelectr Freq Control* 1994;41:314–325.
- O'Donnell M, Flax SW. Phase aberration correction using signals from point reflectors and diffuse scatterers: Measurements. *IEEE Ultrason Ferroelectr Freq Control* 1988;35:768–773.
- Ophir J, Céspedes I, Ponnekanti H, Yazdi Y, Li X. Elastography: A method for imaging the elasticity of the biological tissue. *Ultrasonic Imaging* 1991;13:269–279.
- Patil AV, Garson CD, Hossack JA. 3D prostate elastography: algorithm, simulations, and experiments. *Phys Med Biol* 2007;52:3643–3663.
- Ponnekanti H, Ophir J, Huang Y, Céspedes, I. Fundamental mechanical limitations on the visualization of elasticity contrast in elastography. *Ultrasound Med Biol* 1995;21:533–543.
- Ranganathan K, Walker WF. Cystic Resolution: a performance metric for ultrasound imaging systems. *IEEE Ultrason Ferroelectr Freq Control* 2007;54:782–792.
- Righetti R, Ophir J. Axial resolution in elastography. *Ultrasound Med Biol* 2002;28:695–704.
- Righetti R, Srinivasan S, Ophir J. Lateral resolution in elastography. *Ultrasound Med Biol* 2003; 29:101–113.
- Sadda AS. Elasticity theory and applications. New York: Pergamon, 1974:395–428.
- Souchon R, Soualmi L, Bertrand M, Chapelon JY, Kallel F, Ophir J. Ultrasonic elastography using sector scan imaging and radial compression. *Ultrasonics* 2002; 40:867–871.
- Srinivasan S, Kallel K, Souchon R, Ophir J. Analysis of an adaptive strain estimation technique in elastography. *Ultrasonic Imaging* 2002a;24:109–118.
- Srinivasan S, Ophir J, Alam SK. Elastographic imaging using staggered strain estimation. *Ultrasonic Imaging* 2002b;24:229–245.
- Srinivasan S, Kallel F, Ophir J. Estimating the elastographic signal-to-noise ratio using correlation coefficient. *Ultrasound Med Biol* 2002c;28:1521–1534.
- Srinivasan S, Righetti R, Ophir, J., Tradeoffs between the axial-resolution and the signal to noise ratio in elastography. *Ultrasound Med Biol* 2003;29:847–856.
- Thitaikumar A, Ophir J, Krouskop TA. Noise performance and signal-to-noise ratio of shear strain elastograms. *Ultrasonic Imaging* 2005; 27:145–165.
- Varghese T, Ophir J. Estimating tissue strain from signal decorrelation using the correlation coefficient. *Ultrasound Med Biol* 1996;22:1249–1254.
- Varghese T, Ophir J. The nonstationary strain filter in elastography: Part I. Frequency-dependent attenuation. *Ultrasound Med Biol* 1997a;23:1343–1356.
- Varghese T, Ophir J. A theoretical framework for performance characterization of elastography: The strain filter. *IEEE Ultrason Ferroelectr Freq Control* 1997b;44:164–172.
- Viola F, Walker WF. A spline based algorithm for continuous time-delay estimation using sampled data. *IEEE Ultrason Ferroelectr Freq Control* 2005;42:80–93.
- Walker W, Trahey G. A fundamental limit on delay estimation using partially correlated speckle signals. *IEEE Ultrason Ferroelectr Freq Control*, 1995;52:301–308.